RESEARCH PAPER

Nucleus 5:1, 75–84; January/February 2014; © 2014 Landes Bioscience

Single cell correlation fractal dimension of chromatin

A framework to interpret 3D single molecule super-resolution

Vincent Récamier[1,2,*], Ignacio Izeddin[1], Lana Bosanac[1,3], Maxime Dahan[4], Florence Proux[1], and Xavier Darzacq[1,*]

[1]Functional Imaging of Transcription; Ecole Normale Supérieur; Institut de Biologie de l'ENS (IBENS); Inserm U1024; CNRS UMR 8197; Paris, France; [2]Paris Descartes University; Paris, France; [3]Molecular and Cellular Biology Department; University of California; Berkeley, CA USA; [4]Laboratoire Physico-Chimie Curie; Institut Curie; CNRS UMR168; Université Pierre et Marie Curie-Paris; Paris, France

Keywords: chromatin organization, fractals, adaptive optics, super-resolution microscopy, PALM

Chromatin is a major nuclear component, and it is an active matter of debate to understand its different levels of spatial organization, as well as its implication in gene regulation. Measurements of nuclear chromatin compaction were recently used to understand how DNA is folded inside the nucleus and to detect cellular dysfunctions such as cancer. Super-resolution imaging opens new possibilities to measure chromatin organization in situ. Here, we performed a direct measure of chromatin compaction at the single cell level. We used histone H2B, one of the 4 core histone proteins forming the nucleosome, as a chromatin density marker. Using photoactivation localization microscopy (PALM) and adaptive optics, we measured the three-dimensional distribution of H2B with nanometric resolution. We computed the distribution of distances between every two points of the chromatin structure, namely the Ripley *K(r)* distribution. We found that the *K(r)* distribution of H2B followed a power law, leading to a precise measurement of the correlation fractal dimension of chromatin of 2.7. Moreover, using photoactivable GFP fused to H2B, we observed dynamic evolution of chromatin sub-regions compaction. As a result, the correlation fractal dimension of chromatin reported here can be interpreted as a dynamically maintained non-equilibrium state.

Introduction

Chromosomes are meter-long polymers that fold into a micrometric nucleus. Conventional fluorescence imaging of DNA, such as DAPI staining, reveals regions of lower and higher chromatin density. These differences of local chromatin density in the nucleoplasm raise questions about how chromosomes fill the nuclear space. Unfortunately, due to the inherent resolution limits of classical optical microscopy, it has been difficult to quantitatively assess the spatial organization of chromatin by direct visualization methods. How much chromatin organization differs from a random distribution is a subject of heated debate, as it can help confronting different models of chromosome folding with potential consequences in gene regulation.[1,2] One example of such a model is the fractal globule model of chromatin folding, a knotless structure that homogeneously fills the nuclear space.[3] Evidence for this non-random folding of the chromatin was drawn from chromosome conformation capture assays such as Hi-C[4] and fluorescence in situ hybridization (FISH).[5] In Hi-C experiments, the probability of contact P_c between two loci is quantified as a function of the linear genetic distance s along a chromosome. Similarly, in FISH experiments the relative physical distance R between two loci is measured as a function of the linear genetic distance s. Averaging the inter-loci distances between 10 Mb and 100 Mb, FISH measurements showed that $R(s) \propto s^{1/3}$ (see refs. 5 and 6), and Hi-C resulted in $P_c(s) \propto s^{-1}$ (see refs. 4 and 7). These results deviate from the relations expected upon random organization of the genomic material: $R(s) \propto s^{1/2}$ and $P_c(s) \propto s^{-3/2}$, respectively. Hence, the fractal globule model is justified by the existence of power laws; the difference between the power laws exponents observed, and those expected upon random organization qualify an object as fractal.

Since the 1990s numerous efforts have been developed to reveal the fractal nature of single cell chromatin organization in eukaryote nuclei (see refs. 8 and 9 for a review and citations therein). The first set of evidences of the fractal nature of the nucleoplasm came from diffraction patterns of neutron scattering data[10] and by direct visualization of the nucleus with light microscopy. By imaging a May-Grünwald-Giemsa stained nucleus[11] or studying the movement of an inert tracer inside different nuclear compartments,[12] regions of lower and higher density were observed, evaluating a so-called mass fractal

*Correspondance to: Vincent Récamier; Email: vincent.recamier@biologie.ens.fr; Xavier Darzacq; Email: darzacq@ens.fr
Submitted: 29/10/2013; Revised: 05/02/2014; Accepted: 14/02/2014; Published Online: 19/02/2014
http://dx.doi.org/10.4161/nucl.28227

dimension of the nucleus. Unfortunately, a consensus has not been reached for this dimension, with reported values ranging from 2 to 3.[8] The greatest shortcoming of the microscopic assays has been their limitation to two-dimensional imaging. In 2D microscopy images are formed by projecting on a plane the 3D object captured within the depth of focus (typically ~500–1000 nm). With a probability equal to 1, it is impossible to recover a fractal dimension ranging between 2 and 3 from a 2D projection (theorem 6.2 of ref. 13). Therefore, the impact of imaging in 2D is largely under-evaluated in those studies, even though some rescaling methods were proposed.[14] To overcome this limitation in the most straightforward manner, there is a need to acquire the experimental data in 3D. Nevertheless, so far no study has confronted the Hi-C and FISH measured exponents to the fractal dimension retrieved from chromatin distribution in the nucleus.

Photoactivation localization microscopy (PALM)[15] enables to retrieve the organization of proteins with a resolution lower than that imposed by the fundamental diffraction limit of light. Initially developed for 2D imaging, it can be extended to 3D by the induction of astigmatism in the emission optical path.[16] The output of a 3D PALM experiment is the *x*, *y*, and *z* coordinate positions of a labeled protein of interest. Lists of point coordinates or "point patterns" have been studied for decades addressing the question of homogeneity or lack of thereof.[17] The Ripley distribution *K(r)* of a point process is the inter-point distance distribution.[18] These statistics have been recently used for analyzing PALM experiments in the case of specific enriched regions of proteins. When proteins gather in clusters, the *K(r)* distribution of PALM experiments can quantify the ratio of clusterization,[19] as well as the cluster size.[20] Although localization microscopy has been applied to the study of chromatin structure, this was restricted to a 2D projection along the optical axis,[21] therefore preventing any 3D spatial interpretation on chromatin distribution.

Here, we achieved a three-dimensional direct visualization of the chromatin structure with 3D PALM microscopy using adaptive optics.[22] We detail a method to quantify chromatin enrichment at the nanometric length scale in the nucleus of an osteosarcoma human cell line (U2OS). We specifically address histone H2B, one of the 4 core histone proteins forming the nucleosomes which strongly bind to DNA.[23] H2B covers nearly all the cellular DNA fiber and can be used as a density reference for chromatin with super-resolution imaging techniques.[23] We computed the 3D *K(r)* distribution of H2B and found that this protein does exhibit clusterization. Notably, the H2B clusters do not have any specific size within the range of the experimental limits (between 30 nm to 1 μm). Such an observation is coherent with a fractal nature of chromatin organization. To assess the stability of such a structure in live cells, we performed time-lapse microscopy of patterns of photo-activated chromatin[24,25] and found that this organization is very transient.

Our measurement of the correlation fractal dimension[26] of 2.7 for chromatin specifically quantifies the non-homogeneity of physical distances between loci and helps understand part of the compaction of chromosomes that were observed by FISH when the fractal globule model was proposed. It also establishes a benchmark for a rigorous measure of the fractal dimension using PALM microscopy.

Results

PALM images of H2B heterogeneity

In order to directly determine the spatial distribution of chromatin, we performed 3D PALM experiments of H2B tagged with the photoconvertible fluorescent protein Dendra2.[27] We used an adaptive optics system, placed in the emission optical path between the microscope and the recording EMCCD, in order to induce an astigmatism deformation to the point-spread function (PSF) of the detected single molecules (SM). With such controlled deformation, we were able to determine, in addition to the *x* and *y* coordinates, the *z* position of the individual fluorophores within the focal depth of observation.[22] We thus obtained the planar as well as axial position of H2B molecules with a pointing accuracy of ~15 nm and ~30 nm, respectively. The observation was limited in the axial direction to a region of ~1 μm, with a normal distribution of detections along the optical axis (full width at half maximum of ~600 nm) (**Fig. S1**). Typically, we obtained ~500 000 detections of H2B-Dendra2 molecules in one nucleus, within the aforementioned optical depth. For visualization, we represented the planar projection of the H2B distribution density, calculated for all the SM detections as the number of neighbors within a radius of 100 nm (**Fig. 1A**). The number of detections varies from one cell to another due to different levels of expression. In order to be able to compare images from different cells, we displayed the local density normalized to the total number of detections for each cell and adjusted with a factor 1000 for numerical convenience (the units of such a normalized density are therefore $[\rho_N] = \mu m^{-3} \times 10^{-3}$ counts). Such an image representation of the chromatin distribution revealed clusterization patterns notably, but not only, within an annular region of 2 μm from the nuclear envelope. The clusterization and heterogeneity of H2B distribution is blatant when compared with an image where the same amount of detections have been randomized within the nuclear volume, followed by the same image processing method (**Fig. 1B**)

The outcome of single-molecule based super-resolution microscopy experiments are lists of coordinates with a given localization accuracy. Points are dimensionless objects, and therefore, the outcome of the representation of point patterns is highly dependent on the chosen image rendering method. When the radius used to calculate the number of neighbors was increased to 1 μm, the H2B clusters were not any longer visible in the image (**Fig. 1C**). Conversely, the H2B enrichment in the proximity of the nuclear membrane became all the more evident when we represented the density, estimated on 50 nm wide annular regions, as a function of the distance to the membrane (**Fig. 1D**). We can thus assert that there exists a degree of local enrichment of H2B in the nucleus and that the corresponding enriched regions can be selectively highlighted by different image rendering methods. We therefore have an indication that H2B distribution cannot be accounted for simply by a random

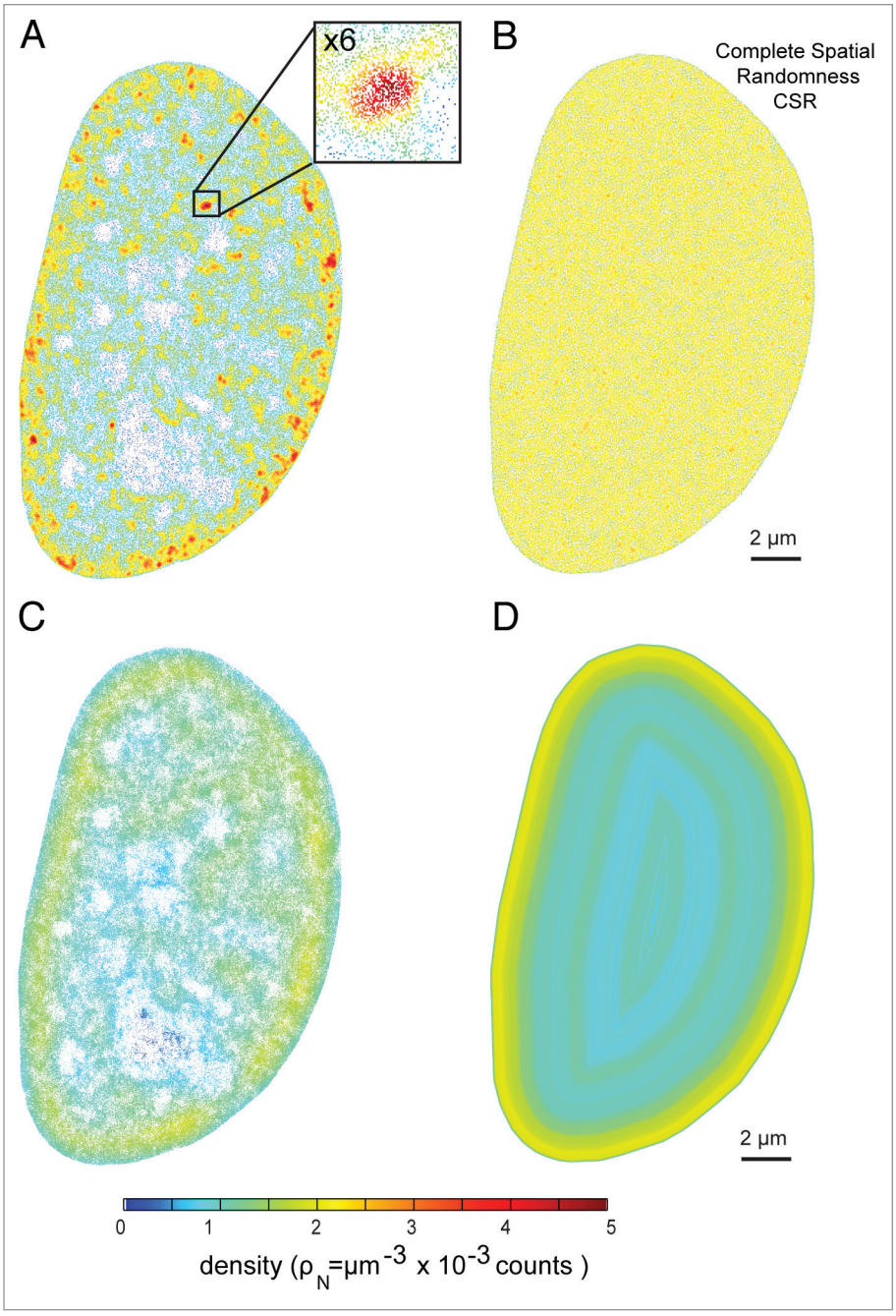

Figure 1. H2B PALM localization inside the cellular nucleus. (**A**) Two-dimensional projection of a 3D PALM acquisition of tagged histone H2B. For each single-molecule detection, the number of neighbors has been calculated within a radius of 100 nm and per unit of volume; the resulting value was normalized by the total number of detections and a factor 1000 for numerical convenience. The color code therefore represents local density with the following units $[\rho_N] = \mu m^{-3} \times 10^{-3}$ counts. In the inset, a zoomed image displaying an intra-nuclear cluster. (**B**) Total number of H2B SM detections spatially re-distributed over complete spatial randomness (CSR) in the nuclear envelope. Here, the same representation procedure as in (**A**) was followed. (**C**) PALM image of histone H2B with local density estimated over a 1 µm radius, showing an enrichment of H2B at the edges of the nucleus. (**D**) Density map estimated over 50 nm wide annular regions defined by their distance to the nuclear membrane.

distribution of clusters of similar size and shape (see ref. 21 for a complete study of H2B heterogeneity in 2D).

The alternation of enriched and depleted regions raises the question of what is the spatial organization of chromatin. The measure of density is misleading in this case because it reflects the region and size of the considered volume (converging to the nuclear average for large volumes) (**Fig. S2**; **Supplementary Text 1**). For that reason, we chose to analyze the distribution of inter-detection distances as a measure of chromatin heterogeneity. The inter-detection distance distribution *K(r)*, also called the Ripley distribution, for single molecule detections of H2B was therefore further investigated to assess the heterogeneity of this

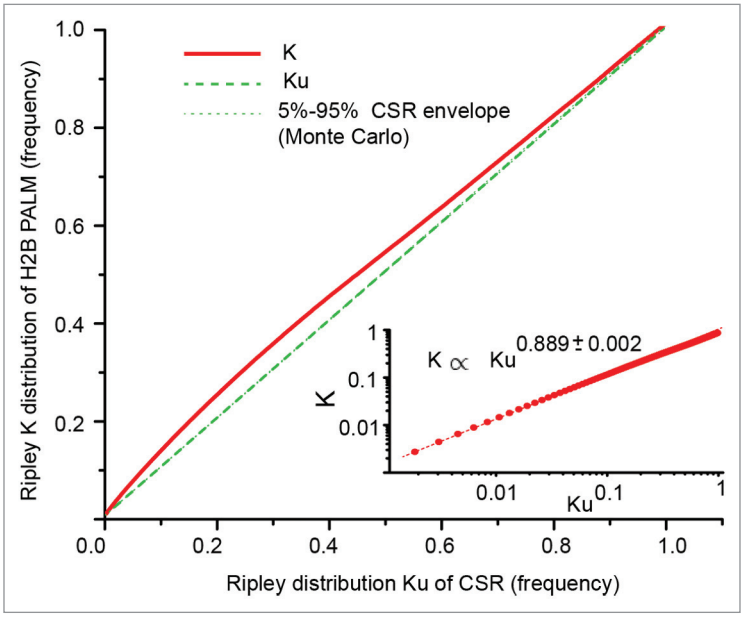

Figure 2. Re-sampling test of H2B distribution against complete spatial randomness (CSR). The Ripley *K(r)* distribution is the number of H2B detections that lie within a circular vicinity of a reference detection, averaged on all possible references. $K_u(r)$ is the Ripley distribution obtained with the total number of detections redistributed in the nuclear volume under complete spatial randomness, averaged over 100 Monte Carlo repeats. For distances "r" between 0 and 3 µm with a 10 nm step, we computed *K(r)* and $K_u(r)$, and plotted *K(r)* against $K_u(r)$. We also plotted the 5% and 95% minimum and maximum quantiles of the Monte Carlo distribution, hardly visible due to the fast convergence of the statistic. As the K statistic never lies in the quantile envelope, the test that the actual distribution of H2B detections could be observed with CSR is rejected at almost every scale at the 10% confidence level. The two distributions *K(r)* and $K_u(r)$ are expected to converge to each other at large scale. However, within the 3 µm range of our study the inset shows a log-log representation that displays a power law dependence between *K(r)* and $K_u(r)$.

list of spatial coordinates or point patterns.[17] It is obtained by choosing a reference point coordinate, counting all the points that lie within a distance *r* of this reference and averaging for all the possible references. If the *K(r)* distribution is then divided by the average density of points of the region of interest, one gets a rescaled function that is invariant upon any stochastic diminution of the number of points, also called thinning.[28] This a crucial characteristic of the *K(r)* distribution function that allows us to analyze PALM data, which, by the nature of the technique, gives us access to a stochastic subset of the total number of H2B molecules. Moreover, such a property makes *K(r)* statistically independent from the level of H2B-Dendra2 expression, and we are therefore able to compare different cells upon this criterion.

Test against complete spatial randomness (CSR)

It has been shown that experimental data resulting in point patterns in biology can be misinterpreted as clustered due to a low pointing accuracy or a poor number of observations.[29] We therefore tested whether the H2B PALM distribution significantly deviates from uniformity. We compared the *K(r)* distribution of the experimental data to that of randomized data, known as complete spatial randomness (CSR)[17] (**Fig. 2**). We took the same number of detections and disposed them randomly in the volume defined by the nuclear envelope, as well as with the same distribution along the optical axis within the focal depth. The shape and amplitude of the distribution probability of SM detections along the optical axis μ_D is highly conserved for different compartments of the cell (**Fig. S1**), since it is determined by the optical system. We therefore used such an axial distribution for the CSR redistribution (see Materials and Methods). We then computed the Ripley distribution of the CSR data for 100 different independent Monte-Carlo realizations.

From this resampling we obtained the reference function $K_u(r)$ and the corresponding 5% and 95% quantiles that define the upper and lower limits of acceptance of uniformity at a particular radius. We restricted ourselves to distances between 0 to 3 µm, estimated within a 10 nm interval, and the latter found that the 3 µm was large enough to detect the heterogeneity of H2B-PALM. From Monte-Carlo resampling, we obtained an envelope for $K_u(r)$ in which we could accept the complete spatial randomness of H2B. Due to a fast convergence of the Ripley statistics, this envelope is hardly distinguishable from the reference $K_u(r)$ (the quantiles are too small to be noticeable in **Fig. 2**). By plotting $(K[r], K_u[r])$ for all the distances "r," that is *K* against K_u, together with upper and lower limit envelopes, we obtain a curve whose deviation from a straight line with slope equal to 1 enables us to compare the experimental spatial organization of H2B to that of the CSR generated data set.

The first observation from the representation of the data in **Figure 2** is that the *K(r)* distribution never lies within the 5–95% envelope around the line $y = x$, showing enrichment at every length scale between 0 to 3 µm. Assuming that H2B distributes homogeneously along the chromatin fiber, we can assert that there is, on average, a local enriched distribution of chromatin in the nucleus.

However, it has been shown that quantifying detections from a PALM acquisition can lead to an overestimation of the numbers of molecules due to the blinking characteristics of photoactivatable fluorophores.[30] This could mislead the analysis to an artifactual conclusion of local enrichment and some algorithms have been proposed to reduce this bias.[31] Here we tested the influence of this overdetection on our analysis aggregating multiple detections within a same region to a single event therefore drastically diminishing the number of detections but greatly reducing the probability to detect the same molecule several times. We then computed the *K(r)* statistic on the resulting subsets of data (**Fig. S3**) and did not observe any significant difference with the original analysis. We could therefore determine that, in our experiments, successive detections of the same molecule and blinking of the fluorophore does not induce a significant deviation to our analysis.

We also implemented several CSR tests on two different cluster distribution models in order to evaluate the validity of our method to assess model specificities (**Fig. S4**). Once the robustness of our analytical approach was validated, we performed additional control experiments on cells transfected with the free fluorophore

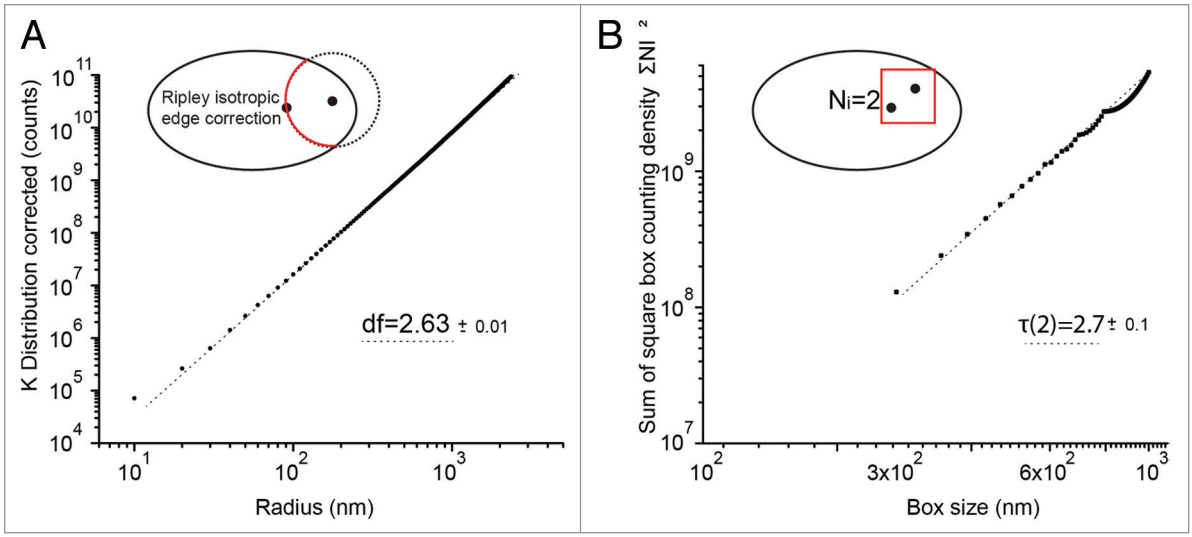

Figure 3. Correlation fractal dimension of H2B distribution. (**A**) Ripley inter-point $\hat{K}(r)$ distribution of H2B corrected for the geometry of the nuclear envelope and the uneven detection probability within the focal depth. $\hat{K}(r)$ displays a power law dependence that can be interpreted as the correlation fractal dimension df of H2B. (**B**) Average square number of detections per cubic boxes, as a function of the box radius. From reference 26, the power law τ(2) is a box counting estimate of the correlation fractal dimension df. The box counting method is less precise, but τ(2) is close to the value *df* that was measured with the Ripley $\hat{K}(r)$ distribution.

Dendra2. Here, the *K(r)* distribution differed substantially from the one obtained for H2B (**Fig. S5**). For Dendra2, we did not observe any enrichment close to the nuclear membrane; interestingly, the nucleoli of the cells were enriched, and the CSR test showed this specific enrichment; lastly, the distribution of Dendra2 outside the nucleoli was homogenous and did not present clusterization or any level of organization.

Interpretation of the CSR test

The *K(r)* distribution has been used in previous studies to compute cluster sizes and distributions on PALM data,[32,20] as well as on electron microscopy data.[33] Cluster models, however, implicitly assume the existence of a cluster class of a given size. We investigated cluster models of H2B distribution and found that, indeed, clusters exist at different scales (**Supplementary Text 2**; **Fig. S6**). Custer interpretation of the *K(r)* function does not hold if the distribution of sizes is scale-less, such as in the case of fractal structures. The relation between *K(r)* and $K_u(r)$ is compatible with a power law. As shown in the inset to **Figure 2** in log representation, a mean least square fit of the scatter plot ([log{*K(r)*},log{$K_\mu(r)$}],$r \in$ [0,3 μm]) yields the dependence $K(r) \propto K_u(r)^{0.889}$. This power law is valid up to 1 μm. After that limit, the convergence of *K(r)* toward $K_u(r)$ as r increases dominates. Due to this power law dependence, $K_u(r)$ obeys different rules of scaling compared with *K(r)*. Unexpected rules of scaling and power laws are mandatory to qualify an object as fractal.[13]

Theoretical fractals are mathematical objects built upon the repetition of simple rules that also exhibit subunits of various sizes.[34] A fractal can be defined by the following properties: (1) a certain degree of self-similarity, (2) an irregular contour, and (3) the existence of a fractal dimension that extends the notion of Euclidean dimension (1D, 2D, and 3D) to non-integer figures.[13] Self-organized fractals are common in nature, and fractals have the very interesting property of summarizing heterogeneity into one single number: the fractal dimension. Typically, a 3D embedded object with a fractal dimension between 2 and 3 will exhibit lacunarities at every length scale, thus never completely filling its environment. The most common mathematical definition of fractal dimension is the Haussdorff dimension *f*, but its exact formulation makes it unusable with a finite data set.[13] Alternative approaches have been proposed to estimate fractal dimensions that are related to the Hausdorff dimension on real data. Among them, the Ripley distribution *K(r)* can give access to the so-called correlation fractal dimension *df* of point patterns.[35]

The test against complete spatial randomness can be a preliminary approach to compute the correlation fractal dimension of H2B. A reasonable assumption is that the complete spatial randomness has a correlation fractal dimension of 3 so that $K_u(r) \propto r^3$, where *r* is the distance between loci. Extending the power law dependence that we have found for H2B, we get that $K_u(r) \propto r^{3 \times 0.889}$, and the correlation fractal dimension of H2B organization is therefore 3 × 0.889 ≈ 2.7. This simple calculation needs further validation, since neither the influence of the confinement nor the spatial range of validity have been assessed. To accept or reject the fractal nature of chromatin, we further extended our analysis with a statistic that is independent from the cell shape.

Correlation fractal dimension

In order to compare the chromatin organization of different cells regardless of their nuclear shape or volume, we treated the nuclear envelope as a restricted region of interest whose geometry needs to be taken into account. As a first adjustment, we used the isotropic correction protocols first introduced by Ripley. The basis of this correction is to weight each pair of detections as a function of their relative distance in the *K(r)* statistic to compensate the bias introduced by the envelope. In our case, the corrected $\hat{K}(r)$

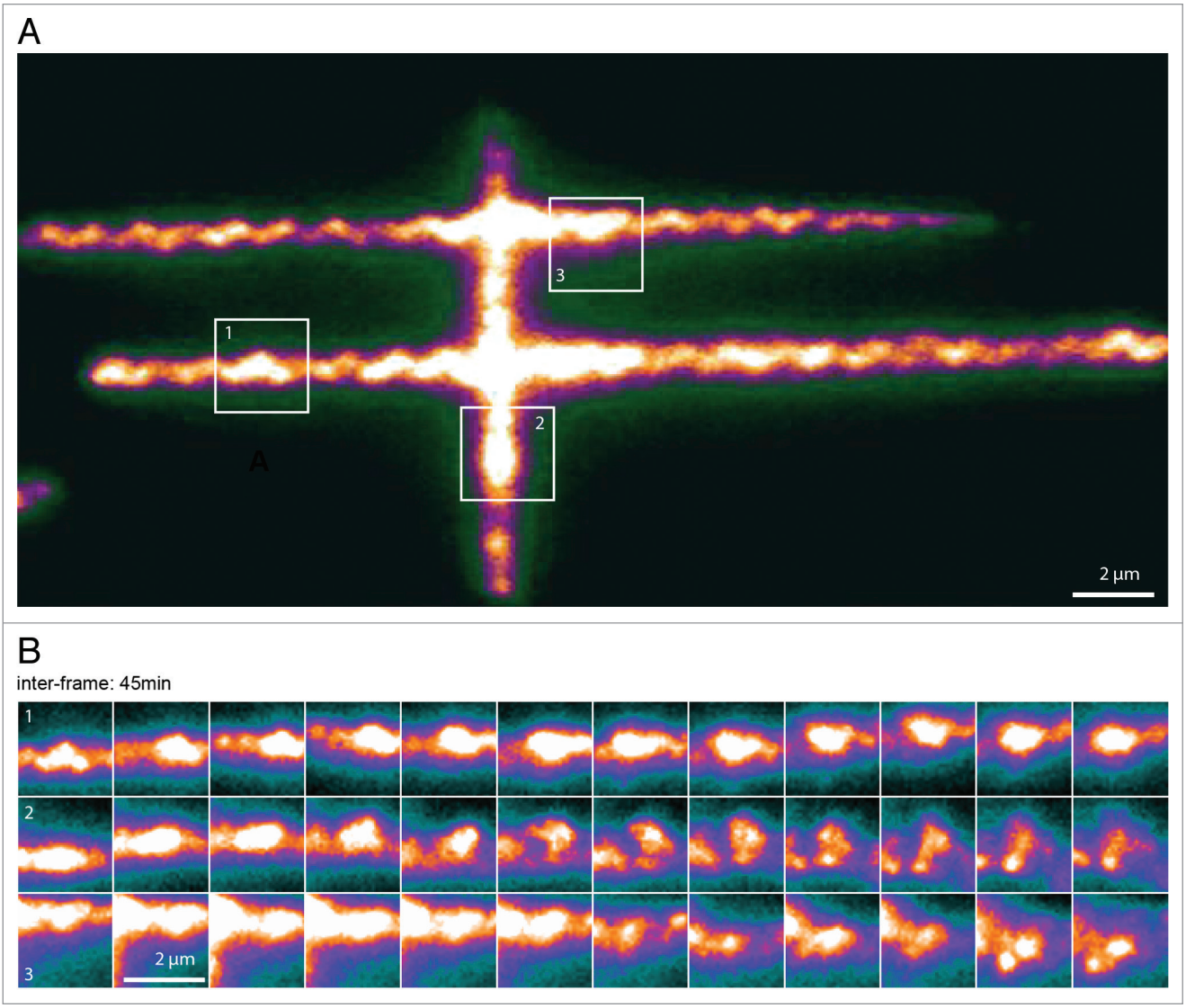

Figure 4. Spatiotemporal evolution of H2B distribution. (**A**) Pattern of photoactivation of H2B labeled with photo-activatable GFP (PA-GFP) in the nucleus of a U2Os cell. (**B**) Time-lapse images of three sub-regions followed over the course of 9 h, showing local condensation and de-condensation of chromatin (image acquisition time, 200 ms; inter frame time, 45 min). See **Video S1** for a complete sequence of this figure.

also includes a correction for the detection distribution in the focal depth along the optical axis (see Materials and Methods). To compute the weights, we need to assume isotropy of the distribution, and the fact that H2B is enriched at the vicinity of the nuclear membrane contradicts this assumption. Despite this limitation, the corrected $\hat{K}(r)$ can be properly fitted with a power law of exponent 2.63 ± 0.05 (**Fig. 3A**). Moreover, both $\hat{K}(r)$ and $K(r)$ scalings are conserved among the cell population with mean and standard deviation 2.69 ± 0.05, in 3 independent experiments (**Figs. S7 and S8**). This value, also very close to the value obtained with the preliminary approach of the CSR test, is therefore a reliable estimate of the correlation fractal dimension *df* of H2B.

An alternative method to retrieve the fractal dimension of a point pattern is "box counting." Cheng and Agterberg showed that the correlation fractal dimension *df* is asymptotically equivalent to the square box counting moment $\tau(2)$.[26] We refer to **Supplementary Text 3** for a detailed definition of $\tau(2)$ in the broader context of multi-fractals, which extends the notion of fractals to densities.[13] In the multi-fractal framework, $\tau(2)$ is only one element of the fractal spectrum (**Fig. S9**). The box counting technique implies dividing the cell volume in 3D boxes. In fluorescence microscopy experiments the restricted focal depth, ~1 µm in our case, is a drastic limitation. We nevertheless obtained the result of the box counting evaluation of $\tau(2)$ for boxes restricted to sizes smaller than 1 µm and larger than 300 nm (**Fig. 3B**). From the log log fit of the box counting curve, we retrieved a value of $\tau(2) = 2.7$ (**Fig. 3B**), which is in very good agreement with the value obtained with the CSR test and the K Ripley distribution, although with lower accuracy.

Dynamics and regulation of H2B organization

From our point pattern analysis of the spatial distribution of H2B in fixed cells, we have seen that the organization of chromatin is not homogenous in the nucleus but rather there is a certain degree of order compatible with a fractal structure. Moreover, we have seen in our experiments that the fractal nature of chromatin folding is stable among the cell population (**Figs. S7 and S8**), but we do not have information about the stability or dynamic rearrangements of the chromatin structure. Yet it has recently been shown, at the single nucleosome level, that the chromatin fiber is indeed flexible and dynamic.[36]

Since super-resolution imaging is not best-suited for long-term live cell imaging, we chose a more qualitative approach to assess chromatin remodeling over time. We transfected cells with H2B tagged with photo-activatable GFP and draw a pattern of photoactivation in the living cell (**Fig. 4A**). This method has been previously applied to monitor chromatin remodeling in the interphase[25] and to monitor ATP dependent rearrangements.[24] We then followed the condensation and de-condensation of different sub-regions of the chromatin fiber for several hours by time-lapse imaging every 15 min (**Fig. 4B**; **Video S1**). We observed substantial changes of local chromatin density, reflecting a constant spatial rearrangement with time. Chromatin is thus spatially self-organized yet transient. The correlation fractal dimension is thus a constant parameter of a dynamically rearranging chromatin structure.

Discussion

With this work we were able to measure the three-dimensional distribution of H2B molecules inside the nucleus of human U2OS cells using PALM microscopy. We confirmed that H2B distribution is heterogeneous in the nucleoplasm, and we could determine that chromatin is organized in regions of enriched density that can be seen at different length scales, from 10 nm to 1 μm (the technical limit of our measure). The single-molecule nature of PALM microscopy allowed us to address the Ripley distribution of H2B, i.e., the distribution of distances between all detected H2B molecules. With these tools we developed an analytical method that revealed that H2B distribution deviates significantly from that of complete spatial randomness. Moreover, this deviation follows a power law whose exponent corresponds to a fractal dimension of 2.7, an invariant value among different cells analyzed.

A chromatin fiber with a spatial distribution of correlation fractal dimension 2.7 exhibits zones of enriched and zones of depleted density. Subsequently, pairs of loci closer to each other than expected upon random organization are enriched. Inter-loci distances measured by DNA FISH between 10 Mb and 100 Mb showed that inter-loci distances were closer than expected upon random organization.[5] Together with Hi-C data, this observation was an additional argument in favor of the fractal globule model. On a fractal globule, the average physical distance $R(s)$ between two loci as a function of their relative genomic distance s scales as a power law: $R(s) \propto s^{1/3}$, which is significantly different from the exponent expected at the equilibrium state, the equilibrium globule, for which $R^{equilibrium}(s) \propto s^{1/2}$. Here, we do not have access to the linear genomic distances, but we can confront the correlation fractal dimension that we obtained with our analysis to the FISH experiments. In **Figure 5**, we used the model inferred by Rosa and Everaers[6] on human chromosome 4 with $R(s) \propto s^{1/3}$, and then unfold it by applying a 3/2 exponent so that we create virtually an equilibrium globule. We then applied the obtained correlation fractal dimension to the relation between the genomic and the linear distance between foci. We found that our correlation fractal dimension can explain part of the deviation that was observed by FISH from $R^{equilibrium}(s) \propto s^{1/2}$. Therefore compaction can contribute to the anomalous scaling of $R(s)$ that was observed by FISH, with no relation to a non-equilibrium nature of polymer folding of DNA.

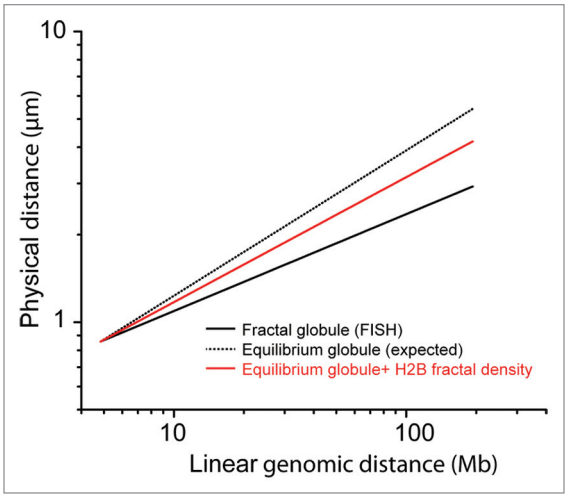

Figure 5. Superposition of H2B fractal density on the FISH model of fractal globule. The fractal globule is a model of conformation of a nuclear DNA with a low level of interminglement. The model can be fit on FISH data of references 5 and 6, with a relation between the physical distance R in the nucleus and the linear genetic distance s along the human chromosome V. This relation scales as a power law $R(s) \propto s^{1/3}$ for long-range interactions (thick black line). By applying a 3/2 exponent, we virtually obtain $R(s) \propto s^{1/2}$, which is characteristic of the equilibrium globule, a model of fully relaxed intermingled nuclear DNA (dotted back line). Finally, by applying a 2.7/3 exponent, we obtain the mean relation of distances between loci in the case a relaxed DNA chain, with a chromatin correlation dimension of 2.7 (red line). This graphic shows that the fractal correlation dimension has a strong impact on the interpretation of FISH measurements used as an additional proof of the validity of the fractal globule model.

Recently, an in silico model of "strings and binders" showed that it could recover the power laws found experimentally. The model consists of treating DNA as a self-avoiding polymer with a given surrounding concentration of DNA-binding proteins.[37] In the "strings and binders" model, the apparent fractal exponents can be explained either by the equilibrium between two segregate states of DNA compaction or a critical concentration of binders that would lead to a fractal organization. Our 3D-PALM data are in favor of a model where chromatin organization is actively maintained by enzymes acting on chromatin compaction.

In our experiments, while every tested cell showed the same correlation fractal dimension of 2.7, our live-cell assay showed that this organization is the result of a highly dynamic system. Chromatin organization thus presents strong local scale mobility yet a stable organization at larger scale. Also, the stability of such a large-scale chromatin organization is strong enough to prevent relaxation to the equilibrium during the cell cycle.[38] It is therefore reasonable to assume that there is an active process that maintains the integrity of the fractal organization of chromatin in such an out-of-equilibrium state. Active remodelers and DNA interacting factors would account for such a role, and the micrometric compaction and de-compaction we observed is likely to be produced by the attachment and release of a pool of DNA interacting factors. Among the processes that could be responsible for this constant exchange, transcription likely plays a major role, as it is one of the main energy consuming process in the nucleoplasm.

Materials and Methods

Cell culture, transfection, and sample preparation

U2OS (Human Osteosarcoma) cells were grown in DMEM (Life Technologies) with 1 g/l glucose and glutamax supplemented with 10% FBS (Fetal Bovine Serum, Life Technologies) and 1% Penicillin/Streptomycin (Life Technologies) at 37 °C with 5% CO2. Forty-eight hours prior to fixation, cells were seeded at 30–40% confluence on plasma-cleaned (2 mn with air with Femto model, Diener Electronic) and collagen-coated (Collagen I from Rat tail, Life Technologies) coverslips (N°1 25 mm).

Plasmid H2B-pDendra2(N) was obtained by cloning H2B coding sequence into pDendra2-N vector (evrogen). Cells were transfected 24 h before imaging with the H2B-pDendra2(N) plasmid (100 ng/25 mm coverslip) using Fugene 6 (Roche Applied Science, IN46250-0414) according to manufacturer instructions. Fixation was performed using para-formaldeïd (4%) (Electron Microscopy Sciences #15714) for 15 min before washing and imaging in PBS.

3D PALM imaging

PALM microscopy was performed on an inverted microscope Nikon Ti Eclipse, with a high numerical aperture objective (1.49 NA) and 100× magnification; extra magnification of 1.5× was used in the tube lens of the microscope, resulting in a total magnification of 150×. We also used a perfect focus system (Nikon) designed to avoid drift on the Z-axis (focus) of the objective, relative to the coverslip. The excitation (561 nm) and activation (405 nm) laser beams were injected into a fiber and focused in the back focal plane of the objective, using an appropriate dichroic (Di01-R561-25x36). Fluorescence emission from individual Dendra2 molecules was filtered with a single band emission filter centered at 607 nm and a bandpass of 25 nm, and recorded on an EMCCD camera (iXon 897).

Once an ROI was selected from the pre-converted (Dendra2 green-form) fluorescence imaging of the live cells, movies of several thousands of frames were acquired under continuous 405 nm and 561 nm illumination (typically 50 000 frames per cell). Drift was corrected using 100 nm beads disposed on the coverslip.

To determine the z position of the molecule, we used an adaptive optics systems consisting of a deformable mirror (Imagine Optics) to correct aberrations and induce astigmatism to the point spread function.[22] We used a modified version of the multi-trace tracking (MTT) algorithm[39] to detect the H2B molecules and fit the signal with an asymmetric 2D Gaussian. We computed the x and y position with 10–20 nm precision and, using a calibration curve obtained with 100 nm beads, the z position of the molecules with an accuracy of 20–30 nm.[22]

Image analysis and statistic computation were performed using Matlab and Mathematica.

Focal depth and Z correction

The distribution of H2B detections along the z axis, $\mu_D(z)$, is determined by the focal depth of the optical system. $\mu_D(z)$ is the convolution between the real distributions of positions $\mu(z)$ and a detection bias that favors positions in the focal plane of the camera. This detection bias varies from one experiment to another as a function of the noise level, but is remarkably stable among different regions of the cell (**Fig. S1**).

As we were acquiring the position of H2B molecules on a large area, the best assumption is the stationarity of the point pattern in the z direction so that $\mu_D(z)$ is the best estimator of $\mu(z)$.[40] We assumed that this distribution $\mu_D(z)$ is independent of the real distribution of the molecule position $\mu(x,y,z)$ that we would have obtained without this bias. We concluded, using the Bayes theorem, that:

$$\mu'(x,y,z) = \frac{\mu(x,y,z)}{\mu_D(z)} \qquad (1.1)$$

where $\mu'(x,y,z)$ is the measured distribution of H2B detections in the nucleus.

In order to determine the position of the CSR point pattern, one needs to define the boundaries of the distribution. In the z direction, the distribution was drawn according to the selection bias $\mu_D(z)$. In the x-y plane, the limit of the cell was defined as the convex envelope of the *z* projected PALM image of H2B with 10 nm binning and a 10 nm opening and closure of the image to exclude isolated detection. Complete spatial randomness points were drawn from the distribution $\mu_u(x,y):\mu_D(z)$ where $\mu_u(x,y)$ is uniform inside the convex envelope. The density measurements of the box counting method were subsequently corrected using $\mu(x,y,z)$ instead of $\mu'(x,y,z)$.

Isotropic correction of the *K(r)* distribution

The *K(r)* distribution is an ever-increasing function, sensitive to pointing accuracy[41] and highly dependent of the embedding volume. The latter can be clearly observed when considering a point pattern randomly distributed in a circular or spherical domain of radius R. In that case the *K(r)* function exhibits a saturation behavior at distance *R/(D+1)*, where D is the embedded dimension 2 or 3, for the circular and the spherical case respectively.[41] In order to compare the chromatin organization of different cells regardless their nuclear shape or volume, we treated the nuclear envelope as a restricted region of interest and

corrected our measurement with rescaling weights. We used the isotropic correction protocols first introduced by Ripley[18] but in 3D, weighting each pair *(i,j)* of detections as a function of their relative distance $|i-j|$ in the *K(r)* statistic to compensate the bias introduced by the envelope and the focal depths.

We assume that the cell boundaries are independent from the z direction so that the theoretical weights can be expressed in the following way, as modified from reference 26:

$$W_{ij} = \frac{\int_{r=-|i-j|}^{|i-j|} w_{ij} \times 2\pi r \times \mu_D(i+r)\,dr}{4\pi |i-j|^2} \quad (1.2)$$

where W_{ij} is the Ripley isotropic weight in 2D. The correction is very time consuming and is to be made on all the pairs of H2B detections. To overcome this problem, we pre-estimated those weights and stored them as an image before computing the corrected $\hat{K}(r)$ statistic. We used the Ripley weight on a 10 nm pixel 2D image of the envelope as a template. The 2D weights W_{ij} were estimated by the convolution of the binary image of the nuclear envelope with a circular mask for increasing radiuses between 10 nm and 3 µm with an increment of 10 nm. Nanometric sensitivity of w_{ij} was obtained by interpolation. We approximated the integral of equation 2 by a sum with 10 nm increment. Those manipulations decreased significantly the computation time, since most weight of the estimation was stored in images. However, as the Ripley weights increase quadratically as a function of the distance to the focal plane, we had to restrict our analysis to a region where they are not too big to smooth all heterogeneity. We chose the reference point *i* of the *K(r)* distribution to a region where the z distribution is relatively high, within the 100 nm peak of the distribution.

Disclosure of Potential Conflicts of Interest

No potential conflict of interest was disclosed.

Acknowledgments

Authors would like to thank Leonid Mirny, Raphaël Voituriez, and Yitzhak Rabin for fruitful discussions. V.R. acknowledges the Fondation pour la Recherche Medicale (FRM) for financial support. We thank Nikon France, ANR-12-BSV8-0015, ANR-11-RPIB-0011, and ANR-10-LABX-54 MEMO LIFE/ANR-11-IDEX-0001-02 for financial support.

Supplemental Materials

Supplemental materials may be found here:
www.landesbioscience.com/journals/nucleus/article/28227

References

1. Fraser P, Bickmore W. Nuclear organization of the genome and the potential for gene regulation. Nature 2007; 447:413-7; PMID:17522674; http://dx.doi.org/10.1038/nature05916
2. Markaki Y, Gunkel M, Schermelleh L, Beichmanis S, Neumann J, Heidemann M, Leonhardt H, Eick D, Cremer C, Cremer T. Functional nuclear organization of transcription and DNA replication: a topographical marriage between chromatin domains and the interchromatin compartment. Cold Spring Harb Symp Quant Biol 2010; 75:475-92; PMID:21467142; http://dx.doi.org/10.1101/sqb.2010.75.042
3. Grosberg A, Rabin Y, Havlin S, Neer A. Crumpled Globule Model of the Three-Dimensional Structure of DNA. [EPL]. Europhys Lett 1993; 23:373-8; http://dx.doi.org/10.1209/0295-5075/23/5/012
4. Lieberman-Aiden E, van Berkum NL, Williams L, Imakaev M, Ragoczy T, Telling A, Amit I, Lajoie BR, Sabo PJ, Dorschner MO, et al. Comprehensive mapping of long-range interactions reveals folding principles of the human genome. Science 2009; 326:289-93; PMID:19815776; http://dx.doi.org/10.1126/science.1181369
5. Sachs RK, van den Engh G, Trask B, Yokota H, Hearst JE. A random-walk/giant-loop model for interphase chromosomes. Proc Natl Acad Sci U S A 1995; 92:2710-4; PMID:7708711; http://dx.doi.org/10.1073/pnas.92.7.2710
6. Rosa A, Everaers R. Structure and dynamics of interphase chromosomes. PLoS Comput Biol 2008; 4:e1000153; PMID:18725929; http://dx.doi.org/10.1371/journal.pcbi.1000153
7. Mirny LA. The fractal globule as a model of chromatin architecture in the cell. Chromosome Res 2011; 19:37-51; PMID:21274616; http://dx.doi.org/10.1007/s10577-010-9177-0
8. Bancaud A, Lavelle C, Huet S, Ellenberg J. A fractal model for nuclear organization: current evidence and biological implications. Nucleic Acids Res 2012; 40:8783-92; PMID:22790985; http://dx.doi.org/10.1093/nar/gks586
9. Metze K. Fractal dimension of chromatin: potential molecular diagnostic applications for cancer prognosis. Expert Rev Mol Diagn 2013; 13:719-35; PMID:24063399; http://dx.doi.org/10.1586/14737159.2013.828889
10. Lebedev DV, Filatov MV, Kuklin AI, Islamov AKh, Kentzinger E, Pantina R, Toperverg BP, Isaev-Ivanov VV. Fractal nature of chromatin organization in interphase chicken erythrocyte nuclei: DNA structure exhibits biphasic fractal properties. FEBS Lett 2005; 579:1465-8; PMID:15733858; http://dx.doi.org/10.1016/j.febslet.2005.01.052
11. Adam RL, Silva RC, Pereira FG, Leite NJ, Lorand-Metze I, Metze K. The fractal dimension of nuclear chromatin as a prognostic factor in acute precursor B lymphoblastic leukemia. Cell Oncol 2006; 28:55-9; PMID:16675881
12. Bancaud A, Huet S, Daigle N, Mozziconacci J, Beaudouin J, Ellenberg J. Molecular crowding affects diffusion and binding of nuclear proteins in heterochromatin and reveals the fractal organization of chromatin. EMBO J 2009; 28:3785-98; PMID:19927119; http://dx.doi.org/10.1038/emboj.2009.340
13. Falconer K. Fractal Geometry: Mathematical Foundations and Applications. 2nd ed. Wiley; 2003.
14. Lee C, Kramer TA. Prediction of three-dimensional fractal dimensions using the two-dimensional properties of fractal aggregates. Adv Colloid Interface Sci 2004; 112:49-57; PMID:15581554; http://dx.doi.org/10.1016/j.cis.2004.07.001
15. Betzig E, Patterson GH, Sougrat R, Lindwasser OW, Olenych S, Bonifacino JS, Davidson MW, Lippincott-Schwartz J, Hess HF. Imaging intracellular fluorescent proteins at nanometer resolution. Science 2006; 313:1642-5; PMID:16902090; http://dx.doi.org/10.1126/science.1127344
16. Huang B, Wang W, Bates M, Zhuang X. Three-dimensional super-resolution imaging by stochastic optical reconstruction microscopy. Science 2008; 319:810-3; PMID:18174397; http://dx.doi.org/10.1126/science.1153529
17. Diggle PJ. Statistical Analysis of Spatial Point Patterns. 2nd ed. Hodder Education Publishers; 2003.
18. Ripley BD. Spatial Statistics. Wiley-Interscience; 2004.
19. Owen DM, Rentero C, Rossy J, Magenau A, Williamson D, Rodriguez M, Gaus K. PALM imaging and cluster analysis of protein heterogeneity at the cell surface. J Biophotonics 2010; 3:446-54; PMID:20148419; http://dx.doi.org/10.1002/jbio.200900089
20. Williamson DJ, Owen DM, Rossy J, Magenau A, Wehrmann M, Gooding JJ, Gaus K. Pre-existing clusters of the adaptor Lat do not participate in early T cell signaling events. Nat Immunol 2011; 12:655-62; PMID:21642986; http://dx.doi.org/10.1038/ni.2049
21. Bohn M, Diesinger P, Kaufmann R, Weiland Y, Müller P, Gunkel M, von Ketteler A, Lemmer P, Hausmann M, Heermann DW, et al. Localization microscopy reveals expression-dependent parameters of chromatin nanostructure. Biophys J 2010; 99:1358-67; PMID:20816047; http://dx.doi.org/10.1016/j.bpj.2010.05.043
22. Izeddin I, El Beheiry M, Andilla J, Ciepielewski D, Darzacq X, Dahan M. PSF shaping using adaptive optics for three-dimensional single-molecule super-resolution imaging and tracking. Opt Express 2012; 20:4957-67; PMID:22418300; http://dx.doi.org/10.1364/OE.20.004957
23. Matsuda A, Shao L, Boulanger J, Kervrann C, Carlton PM, Kner P, Agard D, Sedat JW. Condensed mitotic chromosome structure at nanometer resolution using PALM and EGFP- histones. PLoS One 2010; 5:e12768; PMID:20856676; http://dx.doi.org/10.1371/journal.pone.0012768
24. Shav-Tal Y, Singer RH, Darzacq X. Imaging gene expression in single living cells. Nat Rev Mol Cell Biol 2004; 5:855-61; PMID:15459666; http://dx.doi.org/10.1038/nrm1494

25. Strickfaden H, Zunhammer A, van Koningsbruggen S, Köhler D, Cremer T. 4D chromatin dynamics in cycling cells: Theodor Boveri's hypotheses revisited. Nucleus 2010; 1:284-97; PMID:21327076; http://dx.doi.org/10.4161/nucl.1.3.11969
26. Cheng Q, Agterberg FP. Multifractal modeling and spatial point processes. Math Geol 1995; 27:831-45; http://dx.doi.org/10.1007/BF02087098
27. Baker SM, Buckheit RW 3rd, Falk MM. Green-to-red photoconvertible fluorescent proteins: tracking cell and protein dynamics on standard wide-field mercury arc-based microscopes. BMC Cell Biol 2010; 11:15; PMID:20175925; http://dx.doi.org/10.1186/1471-2121-11-15
28. Weil W. Spatial Point Processes and their Applications. Berlin: Springer Berlin Heidelberg; 2007.
29. Weston DJ, Adams NM, Russell RA, Stephens DA, Freemont PS. Analysis of spatial point patterns in nuclear biology. PLoS One 2012; 7:e36841; PMID:22615822; http://dx.doi.org/10.1371/journal.pone.0036841
30. Owen DM, Sauer M, Gaus K. Fluorescence localization microscopy: The transition from concept to biological research tool. Commun Integr Biol 2012; 5:345-9; PMID:23060958; http://dx.doi.org/10.4161/cib.20348
31. Sengupta P, Lippincott-Schwartz J. Quantitative analysis of photoactivated localization microscopy (PALM) datasets using pair-correlation analysis. Bioessays 2012; 34:396-405; PMID:22447653; http://dx.doi.org/10.1002/bies.201200022
32. Hsu C-J, Baumgart T. Spatial association of signaling proteins and F-actin effects on cluster assembly analyzed via photoactivation localization microscopy in T cells. PLoS One 2011; 6:e23586; PMID:21887278; http://dx.doi.org/10.1371/journal.pone.0023586
33. Prior IA, Muncke C, Parton RG, Hancock JF. Direct visualization of Ras proteins in spatially distinct cell surface microdomains. J Cell Biol 2003; 160:165-70; PMID:12527752; http://dx.doi.org/10.1083/jcb.200209091
34. Mandelbrot BB. Les objets fractals: forme, hasard et dimension. Flammarion; 1975.
35. Ogata Y, Katsura K. Maximum Likelihood Estimates of the Fractal Dimension for Random Spatial Patterns. Biometrika 1991; 78:463-74; http://dx.doi.org/10.1093/biomet/78.3.463
36. Nozaki T, Kaizu K, Pack C-G, Tamura S, Tani T, Hihara S, Nagai T, Takahashi K, Maeshima K. Flexible and dynamic nucleosome fiber in living mammalian cells. Nucleus 2013; 4:349-56; PMID:23945462; http://dx.doi.org/10.4161/nucl.26053
37. Barbieri M, Chotalia M, Fraser J, Lavitas L-M, Dostie J, Pombo A, Nicodemi M. Complexity of chromatin folding is captured by the strings and binders switch model. Proc Natl Acad Sci U S A 2012; 109:16173-8; PMID:22988072; http://dx.doi.org/10.1073/pnas.1204799109
38. Gibcus JH, Dekker J. The hierarchy of the 3D genome. Mol Cell 2013; 49:773-82; PMID:23473598; http://dx.doi.org/10.1016/j.molcel.2013.02.011
39. Sergé A, Bertaux N, Rigneault H, Marguet D. Dynamic multiple-target tracing to probe spatiotemporal cartography of cell membranes. Nat Methods 2008; 5:687-94; PMID:18604216; http://dx.doi.org/10.1038/nmeth.1233
40. Baddeley A. Spatial Point Process Modelling and Its Applications. Castellón de la Plana; Universitat Jaume I; 2004.
41. Kagan YY. Earthquake spatial distribution: the correlation dimension. Geophys J Int 2007; 168:1175-94; http://dx.doi.org/10.1111/j.1365-246X.2006.03251.x